Continental Shelf Research 91 (2014) 82–94

Contents lists available at ScienceDirect

Continental Shelf Research

journal homepage: www.elsevier.com/locate/csr

Research papers

Sea surface height trend and variability at seasonal and interannual time scales in the Southeastern South American continental shelf between 27°S and 40°S

Martin Saraceno [a,b,c,*], Claudia G. Simionato [a,b,c], Laura A. Ruiz-Etcheverry [a,b,c]

[a] Centro de Investigaciones del Mar y la Atmósfera CIMA/CONICET-UBA, Facultad de Ciencias Exactas y Naturales, Universidad de Buenos Aires, Intendente Güiraldes 2160, Ciudad Universitaria, Pabellón II, 2do piso, Ciudad Autónoma de Buenos Aires C1428EGA, Argentina
[b] Departamento de Ciencias de la Atmósfera y de los Océanos DCAO/FCEN, UBA, Facultad de Ciencias Exactas y Naturales, Universidad de Buenos Aires, Intendente Güiraldes 2160, Ciudad Universitaria, Pabellón II, 2do piso, Ciudad Autónoma de Buenos Aires C1428EGA, Argentina
[c] Unité Mixte International UMI IFAECI 3351 CNRS-CONICET-UBA, Facultad de Ciencias Exactas y Naturales, Universidad de Buenos Aires, Intendente Güiraldes 2160, Ciudad Universitaria, Pabellón II, 2do piso, Ciudad Autónoma de Buenos Aires C1428EGA, Argentina

ARTICLE INFO

Article history:
Received 12 September 2013
Received in revised form
2 September 2014
Accepted 2 September 2014
Available online 15 September 2014

Keywords:
Sea surface height
Altimetry
Seasonal cycle
Trend
Rio de la Plata estuarine

ABSTRACT

Recent improvements in satellite altimetry data correction terms are encouraging studies of the remote sensed sea level anomalies (SLA) progressively closer to the coast and over shallow continental shelves. In this paper we describe and discuss the SLA trend and variability at seasonal and interannual time scales in the southeastern South American continental shelf influenced by the Río de la Plata estuary and the Patos Lagoon fresh waters. The spatio-temporal coverage of the gridded altimetry SLA data allows identify several variability patterns and the associated physical processes. On seasonal time scales, the combination of the solar radiation and wind forcing cycles accounts for up to 98% of the variability. Seasonal variability of the wind is responsible for a difference of up to 16 cm between the southern (Argentinean) Río de la Plata estuary coast and the Uruguayan and southern Brazilian coasts. On interannual time scales, positive/negative SLA anomalies are coherent with El Niño/La Niña events. Finally, a significant positive trend of up to 5 mm yr^{-1} is found in all the study area except in the region around the Patos Lagoon (Brazil) and part of the Río de la Plata. Besides the local relevance of the results, this study indicates that satellite altimetry data are accurate enough to unveil SLA spatio-temporal patterns close to the coast and over continental shelves in the mentioned time scales.

1. Introduction

1.1. Motivation

Satellite radar altimetry has a large impact in our knowledge of the oceans. Since the launching of TOPEX/Poseidon (TP) in 1992, the precision achieved by satellite altimetry missions has turn the collected data into a useful tool to study oceanographic processes in the open ocean. Over continental shelves and close to the coast, however, the aliasing of unresolved high-frequency signals is a source of long-wavelength errors that must be corrected to make altimetry measurements useful. Tides and atmospheric forcing are the main processes that generate high frequency signals closer to the coast and over continental shelves. Two examples of high-frequency atmospheric process are winds and tropospheric humidity, both of them having very different signals close to the coast than in the open ocean. Accurate modeling of those components is necessary to avoid important aliasing in the altimetry data. Volkov et al. (2007) showed that using improved corrections, gridded altimetry data provided by AVISO (Archiving, Validation and Interpretation of Satellite Oceanographic data) can be successfully used to study the sea level variability over continental shelves in scales corresponding to periods longer than 20 days. Over the Argentinean continental shelf, which is part of the region selected for this work, Saraceno et al. (2010) estimated the accuracy of different tidal models and showed that north of 42°S tides estimated by the tidal model used by AVISO compares well to tides derived from *in-situ* measurements. Another important aspect is that the space and time scales of oceanic dynamical structures are usually smaller in shallow waters. Thus, the interpolation of along-track data collected by just one or two satellites provides only marginal resolution of the mesoscale and smaller-scale features of ocean circulation (Chelton and Schlax, 2003; Le Traon and Dibarboure, 2002; Leeuwenburgh and Stammer, 2002), which are dominant in the coastal regions.

It is probably due to the above-mentioned difficulties that satellite SLA has not been used before to study the sea level

* Correspondence author.

http://dx.doi.org/10.1016/j.csr.2014.09.002
0278-4343/

variability in the continental shelf of southeast South America. However, Ruiz-Etcheverry et al. (2014) show that at seasonal and longer time-scales gridded SLA satellite altimetry data compares very well to tide gauges (root mean square differences lower than 2.1 cm) in the region. Moreover, as we show in this article, the spatio-temporal coverage of the gridded altimetry SLA data allows identifying several patterns in the region and linking them to physical processes.

1.2. Area of study

The area studied in this work spans from 27 to 40°S and from 47 to 60°W (Fig. 1). Since we are interested in processes occurring over the continental shelf, we considered the region inshore the 200 m isobath, where the continental shelf-break is located. This part of the shelf is highly impacted by the Río de la Plata (RdP) estuary and Patos Lagoon (PL) fresh water plumes. The RdP and PL discharges contribute to the nutrient, sediment, carbon and fresh water budgets of the South Atlantic Ocean (Framiñan et al., 1999 and references therein, Monteiro et al., 2011), affect the hydrography of the adjacent Continental Shelf, and influence coastal dynamics as far as 23°S (Campos et al., 1999, 2013; Framiñan et al., 1999; Piola et al., 2000).

The RdP is an extensive ($\sim 3.5 \times 10^4$ km^2) and shallow (< 20 m) estuary, located at approximately 35°S (Fig. 1). It has a length of 320 km and, at its mouth, it has a width of 230 km. It drains the second largest basin of South America, formed by the Paraná and the Uruguay rivers, concentrating a fluvial drainage area of 3.1×10^6 km^2. Those rivers contribute to a joint mean runoff of 22,000 m^3 s^{-1}, even though peaks as highs as 90,000 m^3 s^{-1} and as low as 7800 m^3 s^{-1} have been observed in association with the El Niño–Southern Oscillation (ENSO) cycles (Robertson and Mechoso, 1998; Jaime et al., 2002). The runoff to the estuary displays a weak seasonal cycle with a maximum of around 30,000 m^3 s^{-1} in winter and 20,000 m^3 s^{-1} in summer, because the individual cycles of its main tributaries are partially opposed and compensate each other (Nagy et al., 1997). The dynamics of the circulation in the estuary and the propagation of the RdP fresh water plume that flows into the adjacent continental shelf are characterized by a highly dynamic regime, mainly dominated by the winds (Simionato et al., 2006, 2007; Meccia et al., 2009, 2013a; Piola et al., 2005). The plume presents a seasonal meridional displacement controlled by the winds (Guerrero et al., 1997; Simionato et al., 2001). South-westerlies prevail during the austral winter, whereas north-easterlies are dominant in summer (Simionato et al., 2005). In response, the freshwater plume moves to the northeast in the cold season and to the southwest during the warm one (Guerrero et al., 1997). Its northward tip reaches 28°S during the austral winter and 32°S during summer (e.g. Möller et al., 2008; Piola et al., 2005, 2008).

PL is the largest coastal lagoon of Brazil, covering a surface area of over 10,000 km^2. The lagoon is directly or indirectly associated with other two coastal lagoons, Mirim and Mangueira (Fig. 1), conforming the Patos–Mirim lagoon complex. In contrast to the RdP estuary, PL has a narrow mouth of less than 1 km that connects it to the ocean at 32.13°S.

The PL drainage basin area exceeds 200,000 km^2 (Garcia et al., 2003). The mean fresh water discharge to the lagoon is mostly supplied by the Guaíba River (Kjerfve, 1986). Season variations of flow drainage can be observed, ranging from 700 m^3 s^{-1} during summer (late December–March) to up to 3000 m^3 s^{-1} in spring (September–early December) (Monteiro et al., 2011). ENSO highly influences the discharge to the lagoon (e.g. Fernandes et al., 2002; Möller et al., 2009; Pasquini et al., 2012); during El Niño, runoff greatly surpasses the mean outflow discharge of the lagoon,

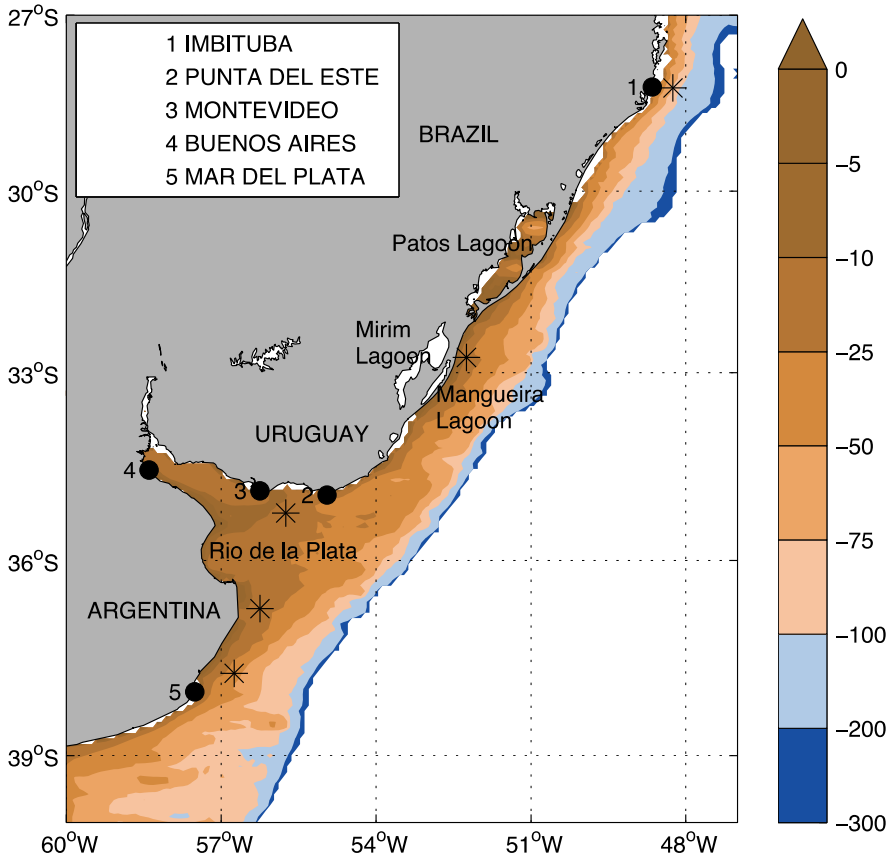

Fig. 1. Bathymetry in meters (Smith and Sandwell, 1997), geographic references, location of the tide gauges (black dots) and positions where the cross-shore component of the Ekman transport was computed (black stars).

sometimes exceeding 25,000 $m^3 s^{-1}$ and making it comparable to the mean RdP runoff. Monteiro et al. (2011) show that PL plume responds to wind variability similarly to the RdP plume, moving northward when winds are from the southwest and southward when they blow from the northeast. In addition to the above described seasonal wind regime, extreme events that cause severe coastal inundations are observed along the southern coasts of the Rio de la Plata in association with SE winds (e.g. Fiore et al., 2009; Framiñan et al., 1999).

Several oceanographic cruises have gathered *in-situ* observations in part of the shelf influenced by the RdP and PL plumes (e.g. Möller et al., 2008; Campos et al., 2013). However, *in-situ* data alone are unable to provide a comprehensive spatio-temporal description of the dynamics of this extensive and dynamical area. In this area satellite observations provide a unique data set to explore the variability of the region. Indeed, much of the results discussed above derived from the analysis of color and SST remote sensed images (e.g. Romero et al., 2006; Piola et al., 2005; Simionato et al., 2010). The aim of this paper is, taking advantage of the almost 20 years of radar SLA satellite observations, to provide a description of the SLA variability at seasonal and interannual time scales and evaluate the involved processes.

1.3. Paper organization

Data and methodology used are described in Section 2. In Section 3 we present the total variance of the SLA and the percentages of that variance which is accounted by the trend, seasonal and interannual components of the SLA; we also discuss the processes that can explain the observed variability. Results are summarized in Section 4.

2. Data sets and methodology

2.1. Sea level data

2.1.1. Satellite altimetry data

Satellite altimetry data used in this paper were constructed by SSALTO/DUACS. We downloaded from the AVISO web site (ftp://ftp.cls.fr) the reference version of the gridded sea level anomaly (SLA) data. The processing of along-track data from altimetric missions into gridded fields of SLA is described in Le Traon et al. (2003). Data are mapped on a 1/3° Mercator projection grid. We extracted the SLA for the region of interest from the global SLA fields for the period 1993–2010 (18 years). The reference version of the altimetry data has the advantage of being constructed using always two simultaneous altimeter missions, one in a 10-day exact repeat orbit (TOPEX/Poseidon, followed by Jason 1 and presently by Jason-2) and the other in a 35-day exact repeat orbit (ERS-1 followed by ERS-2 and then by Envisat). A 7-year (1993–1999) mean SLA is subtracted from the time-series to eliminate the unknown geoid. Data are produced at 7-day and daily intervals. In this work we used both products and, after corroborating that results are not significantly different, the latter are used to allow for a better comparison with other data sets and variables. As discussed by Chelton et al. (2011), this dataset has half-power filter cutoff wavelengths at about 2° in latitude and 2° in longitude. For features with Gaussian shape, this corresponds approximately to an e-folding radius of about 0.4° (Chelton et al., 2011), or 37 km for the mean latitude of the region considered here. As a consequence of the time and space sampling of the satellites described above, gridded altimetry data are limited to solve structures larger than 37 km and with periods longer than 20 days. This is a clear limitation of this dataset to study the coastal region since spatial and temporal scales are often shorter in shallow waters.

2.1.2. Tide gauge data

Monthly sea surface height time series for the locations indicated in Fig. 1 were obtained from the Permanent Service for Mean Sea Level (PSMSL) (Holgate et al., 2013; Permanent Service for Mean Sea Level (PSMSL), 2012). Wherever possible PSMSL used available datum information to tie different records at a location to produce revised local reference (RLR) tide gauge (TG) records. Monthly SLA time series were produced by first correct for the inverted barometer (IB) effect and then subtracting the complete record length mean. The IB correction is a reasonable assumption at seasonal and longer scales considering a pure isostatic response of sea-level to atmospheric pressure variations (Han et al., 1993). The IB correction was applied using sea level pressure (SLP) from the National Center for Environmental Prediction (NCEP) Reanalysis (Kalnay et al., 1996). The SLP database spatial resolution is $2.5^\circ \times 2.5^\circ$. To estimate the IB effect monthly SLP means were calculated at the NCEP grid point closest to the *in-situ* stations.

2.2. Sea surface temperature

We used a blended sea surface temperature (SST) product derived from both microwave and infrared sensors carried on multiple platforms, produced and distributed by the National Oceanic and Atmospheric Administration (NOAA) CoastWatch program (http://coastwatch.pfeg.noaa.gov). The microwave instrument can measure ocean temperatures even in the presence of clouds, though the resolution is a bit coarse when considering features typical of the coastal environment. These are complemented by the relatively fine measurements of the infrared sensors. Measurements are gathered by the Japanese Advanced Microwave Scanning Radiometer (AMSR-E) instrument, a passive radiance sensor carried onboard NASA Aqua spacecraft; the NOAA Advanced Very High Resolution Radiometer (AVHRR) on NOAA POES spacecrafts; the Imager on NOAA GOES spacecrafts, and the Moderate Resolution Imaging Spectrometer (MODIS) on NASA Aqua spacecraft. Data are available at approximately 11 km resolution for the global oceans. The mapping uses simple arithmetic means to produce composite images of 5-day duration. We downloaded the available blended pentads of the SST product that span the period from 12 November 2006 to 6 December 2011. This SST dataset has been successfully used to analyze the variability of the RdP plume from seasonal to sub-annual scales and to detect upwelling events (Simionato et al., 2010). Here we use it to study the seasonal variability of the contribution of the thermosteric effect (i.e. due to the solar-radiative forcing only) to the sea-level change.

2.3. Wind stress

The satellite scatterometer QuikSCAT provided complete coverage of the surface of the ocean from July 20th, 1999 to November 23rd, 2009. We downloaded from the Ifremer web site (www.ifremer.fr/cersat/) a gridded version of the QuikSCAT wind stress at daily temporal resolution and $0.5^\circ \times 0.5^\circ$ spatial resolution. Gridded wind fields were computed by Ifremer from level 2B QuikSCAT scatterometer individual observations provided by JPL/PO.DAAC. Despite of the fact that QuikSCAT database is shorter than the satellite altimetry database, it allows capture small-scale features that are dynamically important to both the ocean and the atmosphere. However, those features are not resolved in other observationally based wind atlases or in NCEP–NCAR reanalysis fields (Risien and Chelton, 2008) that are available for a longer time period.

2.4. Methods

2.4.1. SLA time-scales

For the aim of the analysis, SLA was divided into five components:

(i) *Linear trend*—computed using least square methods.
(ii) *Annual cycle*—computed by harmonic analysis of the detrended signal.
(iii) *Semi-annual cycle*—computed by harmonic analysis of the detrended signal.
(iv) *Interannual variability*—computed as the annual average of the SLA after subtracting the lineal trend and the seasonal cycle.
(v) *Sub-annual variability*—computed as the residual of the SLA after subtracting the trend, the seasonal variability and the interannual variability.

In addition, we defined the *seasonal cycle* as the sum of the annual and the semi-annual cycles.

2.4.2. EOF analysis

We extracted significant modes of variability from the SLA data by computing Principal Components (Empirical Orthogonal Functions-EOF, e.g. Preisendorfer, 1988). EOF analysis can be computed in spatial or temporal mode, referred as S-mode and T-mode (Jolliffe, 2002; Compagnucci et al., 2001). Whereas the S-mode may allow for the identification of homogeneous regions with respect to time variability, the T-mode may be applied with the aim of classifying the spatial fields (Compagnucci et al., 2001). We decided to compute the analysis in S-mode to study the correlations between temporal series. In this mode, the analysis starts with the n ($t=1, 2, \ldots, n$) maps of SLA (z) with m data points (x) and the period-of-record means removed. This original maps are thought as linear combinations of fixed patterns $e_i(x)$ with time-dependent weights $a_i(t)$. Computing the eigenvalues and eigenvectors of the matrix, the maps are decomposed into a linear combination of map patterns; the first pattern explains the most variance, the second is orthogonal to the first and explains the second most variance, etc. This way:

$$z(x,t) = \sum_{i=1}^{N} a_i(t) e_i(x) \tag{1}$$

$$a_i(t) = z^T(x,t) e_i(x) \tag{2}$$

$$e_i(x) = \lambda_i^{-1} z^T(x,t) a_i(t) \tag{3}$$

where N=smaller(m,n); $a_i(t)$ are time series that represent the projections of the maps onto the eigenvectors- they are named either Principal Component (PCs) or factor scores; $e_i(x)$ are maps that represent the eigenvectors of the covariance matrix of z—they are usually named factor loadings; and λ_i are the eigenvalues of the covariance matrix of z. The factor loadings represent the correlation between each PC and the original time-series at every point of the spatial domain. They can be used to identify the regions where the temporal behavior represented by each of the (temporal) PCs is dominant. Thus, the S-mode is useful to perform spatial clusters of the variables. The results correspond to patterns of series that represent the temporal behavior of the variable under analysis in particular regions of the study area. These series, in turn, may be associated with different forcing mechanisms.

2.4.3. Ekman transport

To have a better understanding of the seasonal SLA variability close to the coast we computed the cross-shore component of the Ekman transport (M_x) according to:

$$M_x = \frac{T_y}{\rho_0 f} \tag{4}$$

where T_y is the along-shore component of the wind stress described in Section 2.3, f is the Coriolis parameter and ρ_0 is the density reference value for sea water (1024 kg m^{-3}). Cross-shore transport was estimated by averaging of the above formula along five 50 km sections parallel to the coast and centered at the points indicated in Fig. 1.

2.4.4. Multi-channel singular spectrum analysis

In Section 3 we analyze the multichannel singular spectrum between the Southern Oscillation Index (SOI, http://iridl.ldeo.columbia.edu/) and the SLA measured at the RdP by a TG. Multichannel singular spectrum analysis (M-SSA) is a natural extension of the singular spectrum analysis (SSA, Vautard and Ghil, 1989; Vautard et al., 1992) to a set of time series, in which a grand block matrix containing all pairs of auto- and cross-correlation functions up to a predefined time lag (M) is computed. This matrix contains information on all the dependencies between the different time series. As in SSA, the matrix is decomposed in terms of eigenvectors and eigenvalues. In this case, the method drives to a set of M reconstructed components of each of the series considered (or channels). Depending on the information contained in the cross-correlation matrix, the reconstructed components of different channels may or may not be correlated. If the channels are actually independent, the submatrices corresponding to their cross-correlation equal zero but the submatrix corresponding to auto-correlation does not. So, M-SSA will yield the same results as single-channel SSA. If, however, the cross-correlation submatrix for at least some pair of channels is not null, then M-SSA helps extract common spectral components from the multivariate data set, along with comovements of the channels. M-SSA can usefully analyze only structures with periods in the range (L/5, L) where L is the embedding dimension for the lagged-covariance estimation, e.g. the width, in time units, of an equivalent moving window through the time series (Mann and Park, 1999). The choice of L is critical, and should be chosen among the largest value lower than 1/3 of the record length (N) that contains the period of the structure that we are looking for, if known (Vautard et al., 1992). In our case the time series are 47 years long and of monthly resolution, thus N=564 and L must be smaller than 188 months. We choose L=120 months so we can solve structures with periods in the range [2 10] years, i.e. we can solve typical SOI periodicities. Significant peaks are estimated with the hypothesis of a harmonic process drawn back in a background red noise.

The use of M-SSA for such multivariate time series was proposed theoretically, in the context of nonlinear dynamics, by Broomhead and King (1986). It has been applied to many fields including, for instance, intra-seasonal variability of large-scale atmospheric fields by Kimoto et al. (1991) and Plaut and Vautard (1994), to ENSO in both observed data (Jiang et al., 1995; Unal and Ghil, 1995) and coupled general circulation model (GCM) simulations (Robertson et al., 1995a, 1995b) and to biological time series (Acha et al., 2012). The statistical significance of the SSA pairs was determined by using the Monte Carlo tests against a red noise hypothesis (Allen and Smith, 1996) using 1000 surrogates. All the calculations were done using the SSA-MTM toolkit developed by Dettinger et al. (1995) and Ghil et al. (2002).

3. Results and discussion

3.1. SLA variance: Dominance of the annual and sub-annual variability

The total variance of SLA and the percentages accounted by each of the five components in which the signal was partitioned

(see Section 2.4.1) are shown in Fig. 2. Total variance (Fig. 2f) maximizes at the RdP estuary and at the shelf offshore the PL complex, reaching values up to 330 cm^2. These values are large but lower than those found in open ocean regions where mesoscale activity is responsible for very large eddy kinetic energy values (e.g. in the nearby Brazil–Malvinas Confluence region variance can be as large as 1200 cm^2, Saraceno and Provost, (2012)). Total variance diminishes up to about 80 cm^2 in the intermediate continental shelf and to less than 20 cm^2 towards the continental shelf-break. Thus, SLA total variance clearly highlights the influence of the outflow of fluvial-fresh waters into the continental shelf.

Total variance is mainly explained by the annual cycle (Fig. 2a) and by variability on sub-annual scales (Fig. 2c). The annual cycle accounts for most of the variance offshore the RdP between 34 and 38°S (Fig. 2a), and is significant all along the coast except in the RdP estuary. In contrast, variability on sub-annual scales explains most of the variance in the shallowest zones of the RdP estuary and along the Brazilian continental shelf. The analysis of the variability in short time scales is beyond of the scope of this paper. Satellite SLA in coastal areas must be carefully validated before analyze their temporal and spatial variability at sub-annual time scales. In the shallow RdP it has been shown that SLA variability is dominated by wind forcing on sub-annual time scales (Simionato et al., 2006, 2007, 2010; Meccia et al., 2009). In the deeper part of the Brazilian shelf (north of 32°S) the dominance of variability on sub-annual scales might also be due to oceanic mesoscale activity. The Brazil Current flows southward along the continental shelf break and separates from the coast at about 32°S (e.g. Goni et al., 2011). The baroclinic nature of the Brazil Current (e.g. da Silveira et al., 2004) generates eddies and meanders that might be responsible for the observed sub-annual variability.

In contrast to the annual cycle, variance on the semi-annual time scale (Fig. 2b) is weak, accounting for less than 3% of the total variance in the whole study area. A relative maximum is observed at the outflow of the PL. Even though we could not find references in the literature to the occurrence of a semiannual cycle in this outflow, precipitation in the area display two maxima (in June and September) and two minima (in April and November) along the year (Fig. 2 of Pasquini et al., 2012).

The linear trend (Fig. 2e) accounts for less than 5% of the total variance in most of the study area. Values of up to 22% of the total variance are observed in the outer (offshore) border of the domain south of 36°S.

Finally, variability on interannual time scales accounts for up to an 18% of the total variance in the study area northward 36°S, and in the outer part of the shelf southward that latitude. It explains less than 5% of the total variance in most of the region where the annual cycle maximizes.

In the following sub-sections we explore the possible forcings of the variability at scales longer than the sub-annual.

3.2. Linear trend

Positive trends ranging from 2 to 5 mm yr^{-1} significant at the 99% CL according to the Student-*t* test are found over most of the study area (Fig. 3). The average trend for the whole region is of

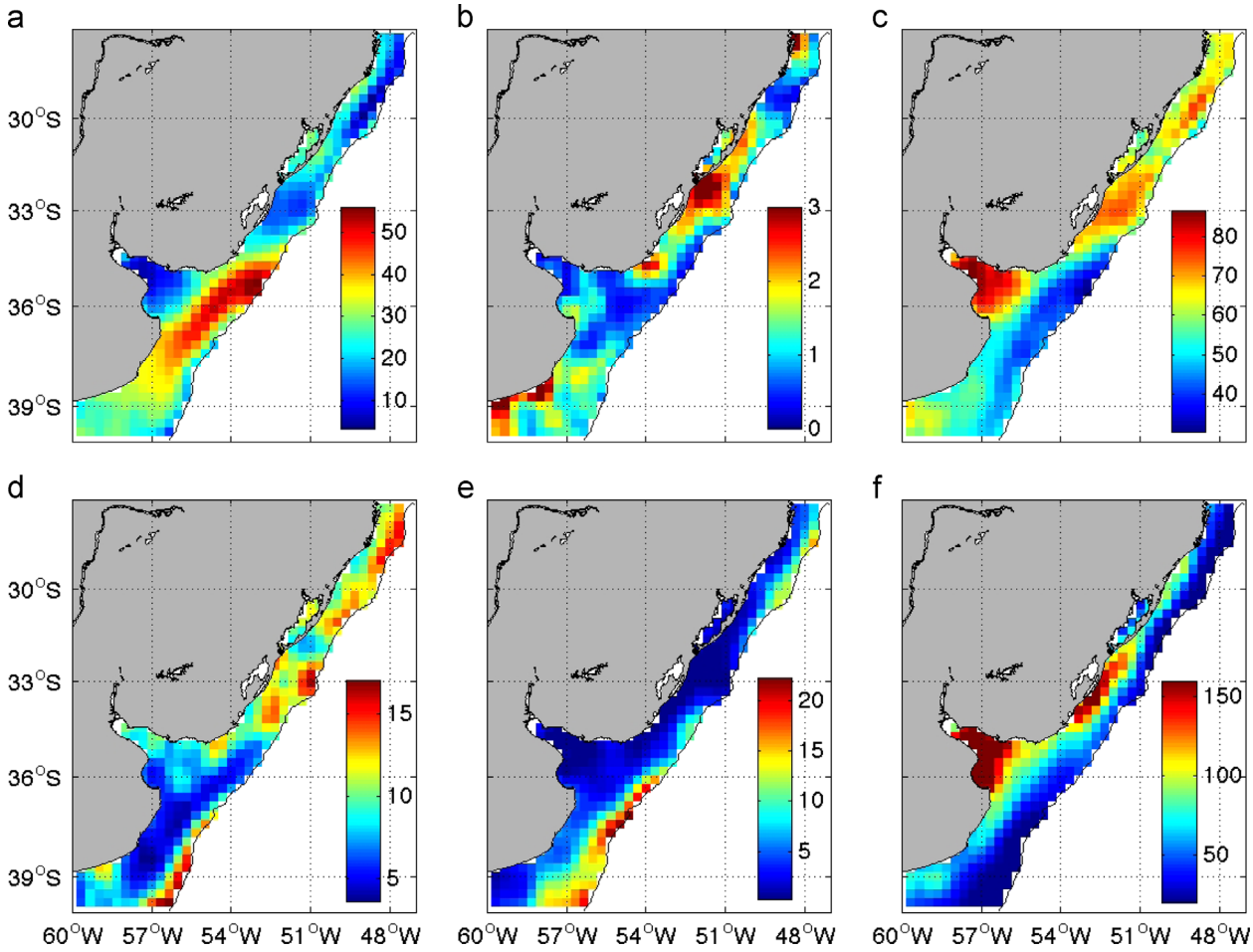

Fig. 2. Total variance (*f*, in cm^2) and percentage of variance explained by the annual cycle (a), semi-annual cycle (b), sub-annual scale (c), interannual scale (d) and trend (e). See text for definitions of the different components.

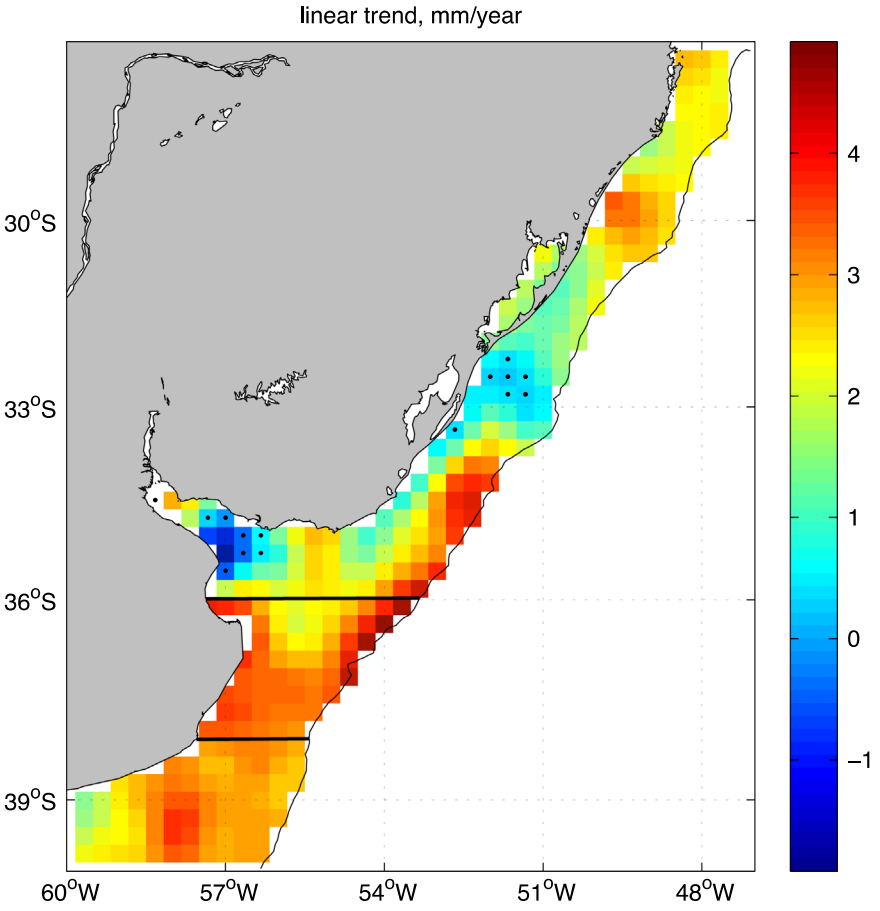

Fig. 3. Linear trend, mm yr^{-1}. Black dots show the locations where the linear trend in not significant at the 99% CL according to Students-*t* test. Black horizontal thick lines, the coastline and the 300 m isobaths (thin black line) delimitates the region used to construct the time series displayed in Fig. 4.

2.5 mm yr^{-1}, a value that is lower than the global average of 3.2 mm yr^{-1} obtained during the altimetry era (e.g. Meyssignac and Cazenave, 2012) but larger than the 1.1 mm yr^{-1} obtained by Wöppelmann et al. (2014) for the southern hemisphere considering observations from the Global Positioning System for the correction of the vertical land motion and a longer period of time.

The largest values are observed in the outer border of the continental shelf, between 34 and 37°S, corresponding to the region influenced by the Brazil and Malvinas currents (e.g. Saraceno et al., 2004). It has been shown that a southward migration of the position of the Brazil current front is ongoing (Goni et al., 2011; Sato and Polito, 2008), probably as a consequence of a southward migration of the semi-permanent anticyclonic high of the subtropical South Atlantic (Barros et al., 2008). Such a migration might, locally, intensify the boundary Brazil Current, which might, in turn, increase the SLA. Indeed Goni et al. (2011), in their Fig. 10, show the SLA linear trend offshore the 200 m isobaths; the latitude range in which they observe maximum positive trends (34 to 37°S) matches ours.

Another region with large positive trend values is observed along the coast, between 36 and 38°S. We argue that this pattern can also be explained as a consequence of the southward migration of the semi-permanent anticyclonic high of the subtropical South Atlantic (Barros et al., 2008): such a migration will increase the frequency of easterlies and northeasterlies which in turn would increment the RdP plume southward extension (Simionato et al., 2004; Meccia et al., 2013b) and thus affect the SLA trend between 36 and 38°S. Using the QuikSCAT time-series we tested that a positive trend of 2.5 days yr^{-2} (95% CL computed considering Student-*t* test) is obtained for the number of days per year for which northeasterlies are dominant between 36 and 38°S (Fig. 4).

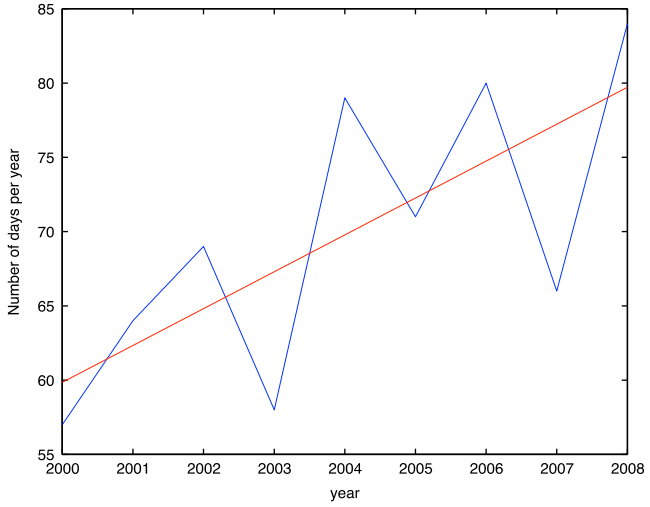

Fig. 4. Blue line: Number of days per year that QuikSCAT wind is from the NE in the region indicated in Fig. 3. A day with winds from the NE is considered when at least 70% of the pixels considered in the region have their wind direction included between 30° and 60°. The mean of the blue line is 68. Complete calendar years are considered. Red line: linear fit of the blue line. (For interpretation of the references to color in this figure legend, the reader is referred to the web version of this article.)

It is worth observing the presence of two spots, in the RdP and in the region offshore the PL outflow, which present negative trend values (Fig. 3). Most of those negative values are non-significant at the 99% CL (Fig. 3). Thus, apart from noting that the location of the negative values suggests the influence of fresh water of continental

origin, we will not further analyze the reasons for the negative trends. Positive, significant values of around 1–2 mm yr^{-1} are observed in the upper RdP estuary and in the northern PL. These results are in good agreement with trend estimates derived from local tide gauge measurements in the upper RdP (Lanfredi et al., 1998; D'Onofrio et al., 2008) and in the PL (Möller and Fernandes, 2010).

3.3. Interannual variability

To favor the analysis of the variability in interannual time scales we computed the PCs of the interannual component of the gridded SLA dataset presented in Section 2. Only the first mode accounts for a large percentage (51%) of the total variance and seems to have a physical meaning. The map of the factor loadings of this leading mode (Fig. 5a) depicts a clear change at about 37°S. North of this latitude, the correlation between the time series of the factor scores associated to this mode (blue line in Fig. 5b) and the interannual component of the SLA are larger than 0.6, whereas southward of 37°S they decay up to 0.3. Largest correlations occur in the regions of influence of the RdP and PL plumes, reaching values close to one at some locations. Therefore, the factor loadings suggest that the leading mode represents interannual variability associated with the impact of fresh waters of continental origin on the shelf.

To provide an idea of the order of magnitude of the SLA associated with this variability pattern, a time series of the interannual SLA from the point marked with a circle in Fig. 5a has been superimposed to Fig. 5b as a green line. Correlation between the first PC mode and the data for that point is 0.84 (Fig. 5a). It can be observed that the interannual SLA signal in the region can be as large as 4 cm (Fig. 5b). During the period 1993–2011 four minima (in 1996, 2000, 2004 and 2008) and four maxima (in 1994, 1998, 2003 and 2005) are observed. The maxima coincide with El Niño events, suggesting a possible teleconnection to ENSO. Indeed, Fig. 5b suggests a negative correlation

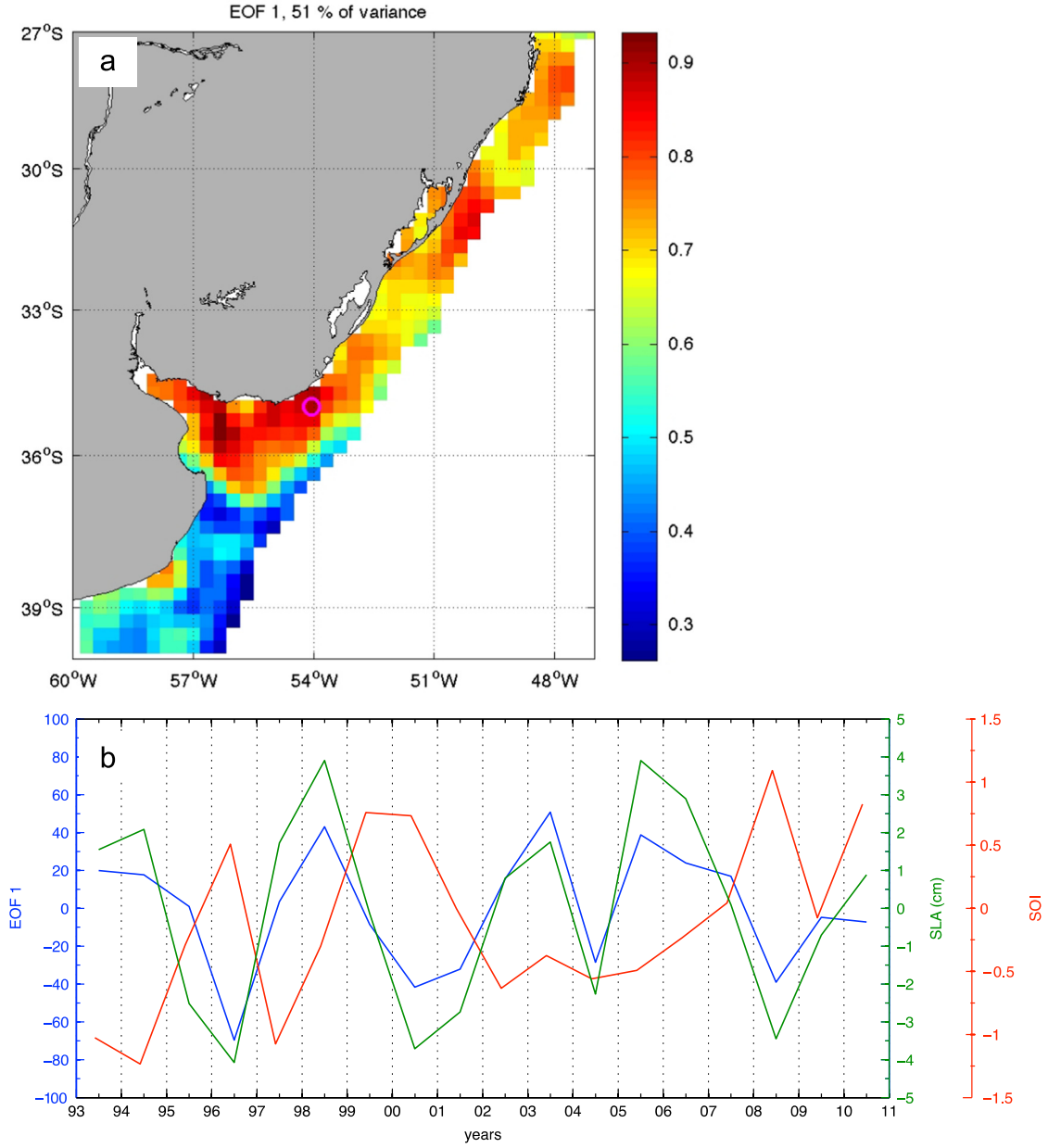

Fig. 5. (a) Factor loading of the first EOF mode of SLA inter-annual variability (see text for definition); (b) Factor score corresponding to the first EOF mode of SLA inter-annual variability (blue line), standardized Southern Oscillation Index (red line), and SLA (cm) extracted at the point indicated with a magenta circle in panel (a) (green line). The three time series have been yearly averaged in panel (b). (For interpretation of the references to color in this figure legend, the reader is referred to the web version of this article.)

between the standardized SOI index (http://iridl.ldeo.columbia.edu/) and the leading PC mode. To verify the relationship between SOI and SLA we considered an independent and longer data record: we searched for common pseudo-periodicities between the 47 years-long time series of SLA collected at the TG of Palermo and the SOI index for the same period of time using the M-SSA methodology (see Section 2.4.4). Both time series were first low-pass-filtered to eliminate periodicities lower than one year. Two significant oscillatory pairs at periods around 2.6 and 3.7 years (95% CL) were found (Fig. 6); they are in the range of typical ENSO periodicities, suggesting that ENSO might affect SLA in the RdP area at interannual time scales. The mechanisms to explain this relationship, expressed by Mode 1, are straightforward: ENSO cycle is known to strongly modify the precipitation regime (e.g. Barros et al., 2008) and, therefore, the rivers runoff in South America (Robertson and Mechoso, 1998; Jaime et al., 2002); For the particular cases of the RdP and PL, when the SOI is positive/negative (negative/positive phase of ENSO) runoff strongly decreases/increases (Robertson and Mechoso, 1998; Pasquini et al., 2012). During those events, the mean wind stress pattern that corresponds to moderate northeasterlies is also modified: easterlies intensify/weaken during El Niño/La Niña events (Meccia et al., 2009). This effect limits in some extent the northward excursion of the RdP and PL plumes along the Uruguayan and southern Brazilian coasts during El Niño years (Piola et al., 2008; Meccia et al., 2009) and, might be, contributes to further enhance the SLA.

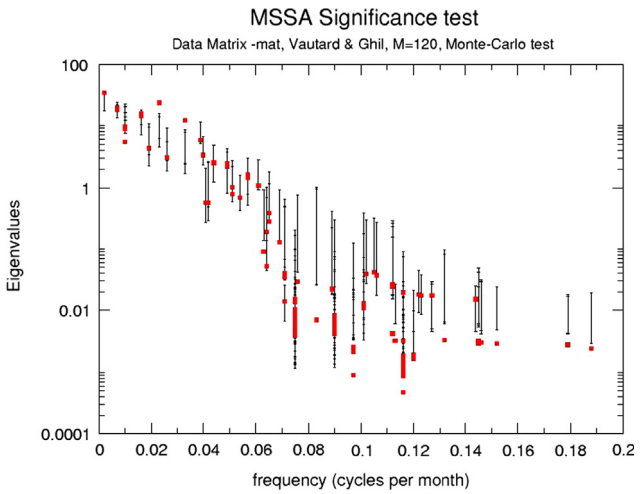

Fig. 6. Red-noise surrogate projections plotted against the dominant frequencies associated with each M-SSA (multichannel singular spectrum analysis) mode between the standardized SOI index and the monthly mean SLA observed in Buenos Aires. The projections of the data are represented by the red dots and the associated eigenvalues can be regarded as significant when they are above the 95% error bars (black vertical lines) representing the null hypothesis of red noise. Please refer to Section 2.4.4 for the parameters used to compute the spectra. (For interpretation of the references to color in this figure legend, the reader is referred to the web version of this article.)

3.4. Seasonal variability

To help on the identification of the different physical mechanisms that can account for the observed cycles, SLA variability on seasonal time scales was also explored by means of PCs. To do this,

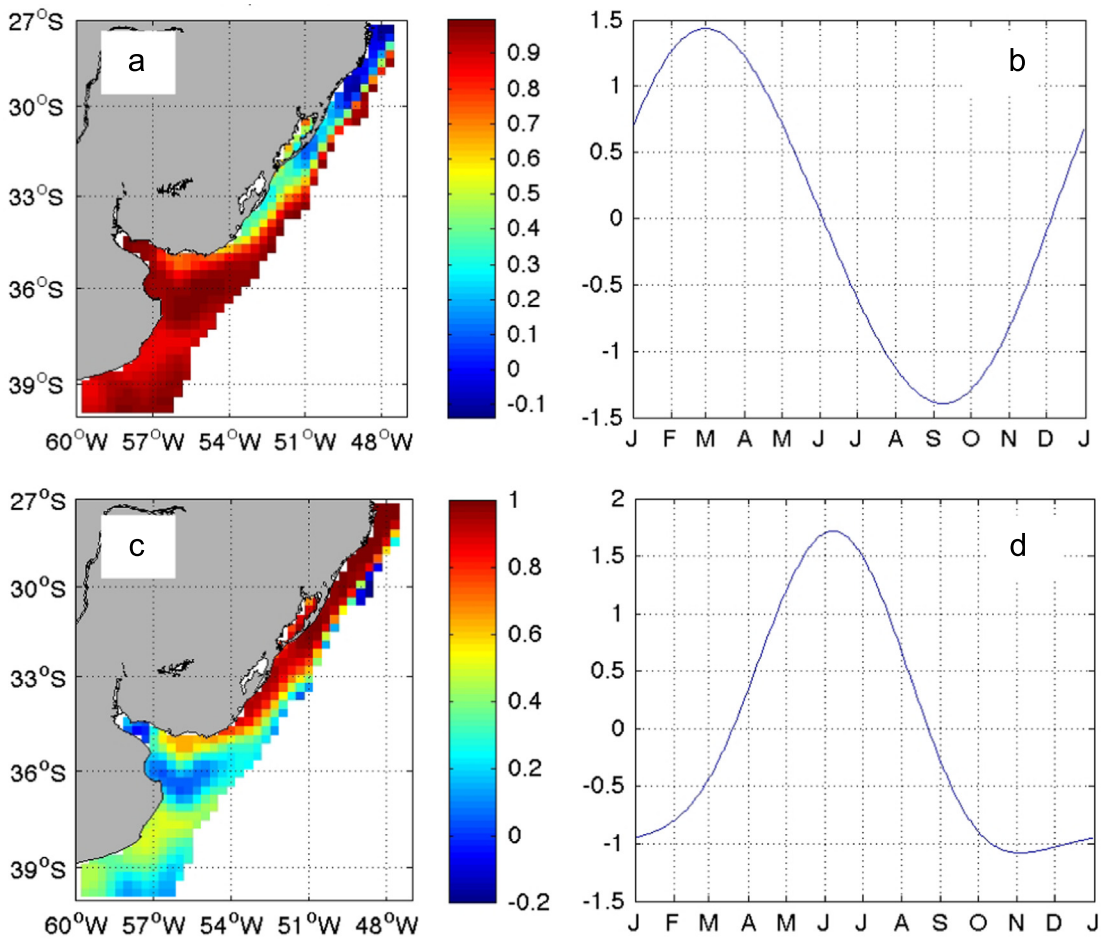

Fig. 7. Leading EOF modes of seasonal variability. Left column: factor loading of the first (*a*) and second (*c*) EOF modes. Right column: factor score corresponding to the first mode (*b*) and second mode (*d*).

the time series at each spatial grid point consists of the reconstructed 2-harmonic seasonal cycle at that point as defined in Section 2.4.1. The first two modes account for 98% of the variance (65% and 33%, respectively; upper and lower panels of Fig. 7). The spatial pattern of the factor loadings (left panels of Fig. 7) shows that both modes are spatially complementary. The factor score of the first mode correlates very well (with values larger than 0.85) to the observations in the shelf south of 35°S and in the outer shelf north of that latitude. In the coastal areas north of 35°S, the second mode displays values larger than 0.85.

The factor score or time series of the first mode (upper right panel of Fig. 7) maximizes in March and minimizes in mid-September suggesting that this mode reflects the solar-radiative forcing. In contrast, the second mode (lower right panel of Fig. 7) maximizes in June and minimizes from mid-September to the end of February. As we will discuss in what follows, this mode represents the effect of the wind forcing on the coastal areas of Uruguay and southern Brazil.

To further explore the seasonal variability of the SLA in the region and better understand the derived PCs (Fig. 7), the amplitude and phase of the annual cycle of SLA and of the SST was calculated using harmonic analysis in the region; results are shown in Fig. 8. The amplitude of the SLA annual harmonic (Fig. 8a) is larger than 6 cm along the coast in most of the study area, excepting northward 28°S. It maximizes in the region of the RdP plume extension, reaching values of up to 9 cm. The annual SST amplitude (Fig. 8b) also displays large values in the area influenced by the RdP and PL plumes. The comparison between the bathymetry (Fig. 1) and SST amplitudes and phases (Fig. 8b and d) shows that (i) SST amplitudes are larger and (ii) the annual maximum peaks at least 20 days before than in the adjacent continental shelf in the shallow RdP estuary and PL. Both observations are coherent with the fact that in shallow regions relatively isolated from oceanic currents solar radiation can warm waters faster and to higher temperatures than in deeper waters more exposed to oceanic currents. Intermediate SST amplitude values (5 to 6 °C) between 30 and 37°S reflect the influence of the warmer RdP plume advected along the continental shelf (e.g. Piola et al., 2005). Significant differences between the amplitude of the annual SLA and SST cycles are observed in two regions: One region corresponds to the shallow areas of the upper RdP estuary and PL, where the SST annual cycle amplitude maximizes and the SLAs amplitudes do not. The second area is located northward PL and southward 38°S, where the amplitude of the SST annual cycle monotonically diminishes towards the north and south respectively, whereas the amplitude of the SLA cycle keeps always large close to the coast.

The spatial distribution of the phase (Fig. 8c and d) of the annual SLA and SST cycles is quite different to that of the amplitude (Fig. 8a and b). The phase of the SLA annual cycle displays a spatial pattern that closely resembles the second PC mode and it is almost opposed to the first one (Fig. 7). Fig. 8c also reveals that the maximum annual SLA occurs progressively later along the year to the north. This happens in late summer (mid-March) in the southern coast of the RdP, but can occur even in late fall (mid-June) along the Brazilian coast northern 30°S. This seems to be indeed the kinematical meaning of the patterns extracted by the PC modes (Fig. 7). For the SST, instead, the behavior is pretty different. The maximum of the annual harmonic occurs during the first days of February in the shallow waters of the RdP and PL, whereas in the rest of the study area it takes place at least 15 days later.

To verify the phase lag of the SLA annual cycle observed in Fig. 8 with an independent data set, Fig. 9 displays monthly climatologies

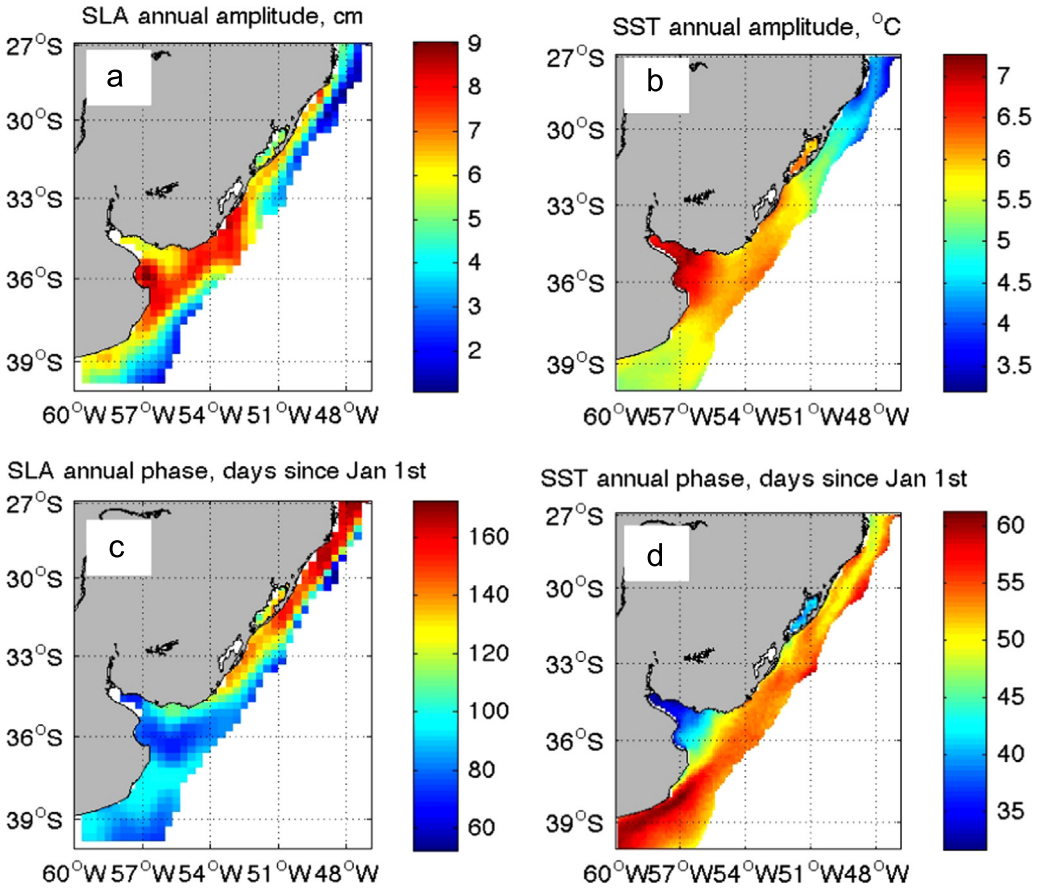

Fig. 8. Amplitude (cm) and phase (days since January 1st) of the seasonal component of the SLA (respectively *a* and *c*) and of the SST (respectively *b* and *d*).

derived from *in-situ* data gathered by five TGs located along the coast. TGs amplitudes and phases displayed in Table 1 were estimated by fitting an annual wave to the climatologies shown in Fig. 9. In general Table 1 shows a good agreement between TGs and Satellite data. There are two locations with a noticeable phase difference: in Buenos Aires the lag is probably due to the fact that there are no pixels with data close to the TG (Ruiz-Etcheverry et al., 2014) while at Punta del Este it is more likely that the satellite captures the open ocean conditions that are more dominated by the radiative solar forcing while the TG at the coast is more dominated by the wind-forcing upwelling regime. Difference between open ocean and coastal conditions at Punta del Este are evident in Fig. 7: the factor score of the 2nd mode, that is related to the wind forcing regime, maximizes only close to the coast at Punta del Este; conversely the factor score of the 1st mode is larger offshore than close to the coast at Punta del Este. The reader is referred to Ruiz-Etcheverry et al. (2014) for a discussion about differences and similarities between the SLA annual signal as retrieved by satellite altimetry and the TGs. Here we note that the phase lag pattern observed in the previous paragraph, i.e. that the SLA annual cycle peaks before in the southern coast of the RdP than in the Brazilian or Uruguay coasts, is consistently retrieved by both TGs and satellite datasets.

Thus, it is evident that the annual cycle of the SLA observed in Figs. 8 and 9 cannot be explained by the radiative solar cycle alone, but there must be another mechanism forcing waters up and down in the proximity of the Uruguayan and Brazilian coasts. As mentioned above, wind stress in the study area displays a marked seasonal cycle: whereas south-westerlies are dominant during autumn-winter, north-easterlies prevail in spring-summer. Note that, in addition, the areas where the seasonal SLA winter maximum is observed (the Uruguayan and Brazilian coasts) are oriented from the northeast to the southwest, well aligned with the dominant winds directions. Therefore, prevailing winds are upwelling favorable during the austral spring-summer and downwelling-favorable in autumn-winter. This might explain not only the period of the year when the maximum annual SLA occurs, but also the large anomalies observed very close to the Uruguayan and Brazilian coasts in the upper panel of Fig. 8.

To assess the influence of wind variability on the SLA in the coastal region we computed the cross-shore Ekman transport per unit width, as discussed in Section 2, at five different segments of the study area centered at the locations shown in Fig. 1. Results, shown in Fig. 10, display several characteristics of the wind-forcing regime that are consistent with our previous inferences:

(i) At all the locations a transition from a dominant downwelling regime during the austral autumn–winter to a prevalent upwelling regime during the austral spring–summer is observed;
(ii) There is an evident difference between the upwelling-downwelling regime along the coast southward and northward the RdP. In the former the upwelling-favorable period lasts for less than 3 and half months (from mid-October to end of February). In the latter, upwelling lasts for at least seven months (from September to end of March). As a consequence, the total amount of upwelled water is much larger along the Brazilian and Uruguay coasts than along the Argentinean coast. Similarly, the amount of downwelled water is larger at the southern locations than at the northern ones (except at 33°S);
(iii) The downwelling-favorable season starts by end of February in the southern (Argentinean) coast, whereas along the Brazilian and Uruguayan coasts that season starts between the end of March and mid April. The 30–45 days lag interval overlaps the 30–80 days lag window observed in the annual SLA phase map derived from satellite data (Fig. 8).

Thus, whereas the first PC mode (upper panel of Fig. 7) represents the effect of the radiative solar cycle on the SLA, the second (lower panel of Fig. 7) is capturing the effect of the marked seasonal cycle of the wind in the area. The factor score of the second mode represents an intermediate situation between the North and South regimes. Such a result is not surprising since the PC was computed considering the whole domain. Evidence of wind-forced upwelling in the northern part of the domain has

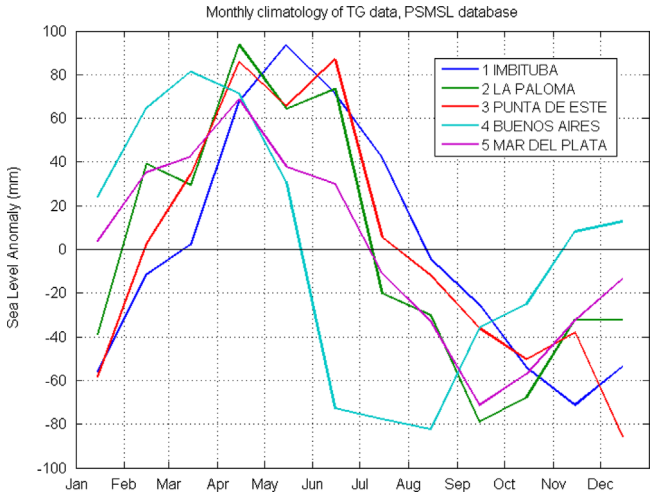

Fig. 9. Monthly climatology of SLA (mm) estimated at the five tide gauge locations indicated in Fig. 1.

Table 1
Amplitude and phases of the annual component of the SLA obtained from five TGs (see locations in Fig. 1) and from the closest pixel of the satellite altimetry dataset.

Tide gauge name	Amplitude (mm)		Phase (days since January 1st)	
	TG	**Satelite**	**TG**	**Satelite**
1. Imbituba	74	55	146	156
2. La Paloma	72	73	119	114
3. Punta del Este	82	75	126	104
4. Buenos Aires	72	60	51	71
5. Mar del Plata	58	57	97	94

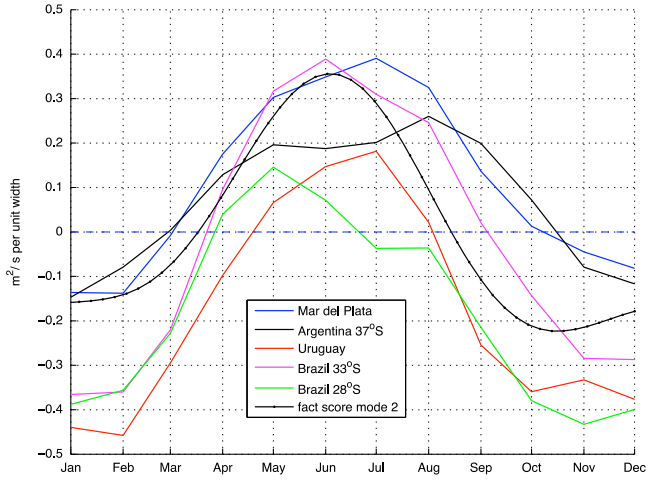

Fig. 10. Ekman transport estimated at the five locations indicated with a star in Fig. 1 (colored lines) and factor score for the second mode of variability of seasonal SLA (black line with dots). The five Ekman transport time series have been multiplied by −1 to easier the comparisons with the factor score. Thus negative (positive) values indicate water removed from (pushed towards) the coast, suggesting wind-forced upwelling (downwelling).

been documented by Möller et al. (2008) using a large number of *in-situ* data and by Campos et al. (2013) using *in-situ*, satellite SST and wind stress fields and a numerical model. East of Punta del Este, several authors have reported upwelling from remote and *in-situ* observations (Framiñan (2005) and references therein; Pimenta et al., 2008; Simionato et al., 2010).

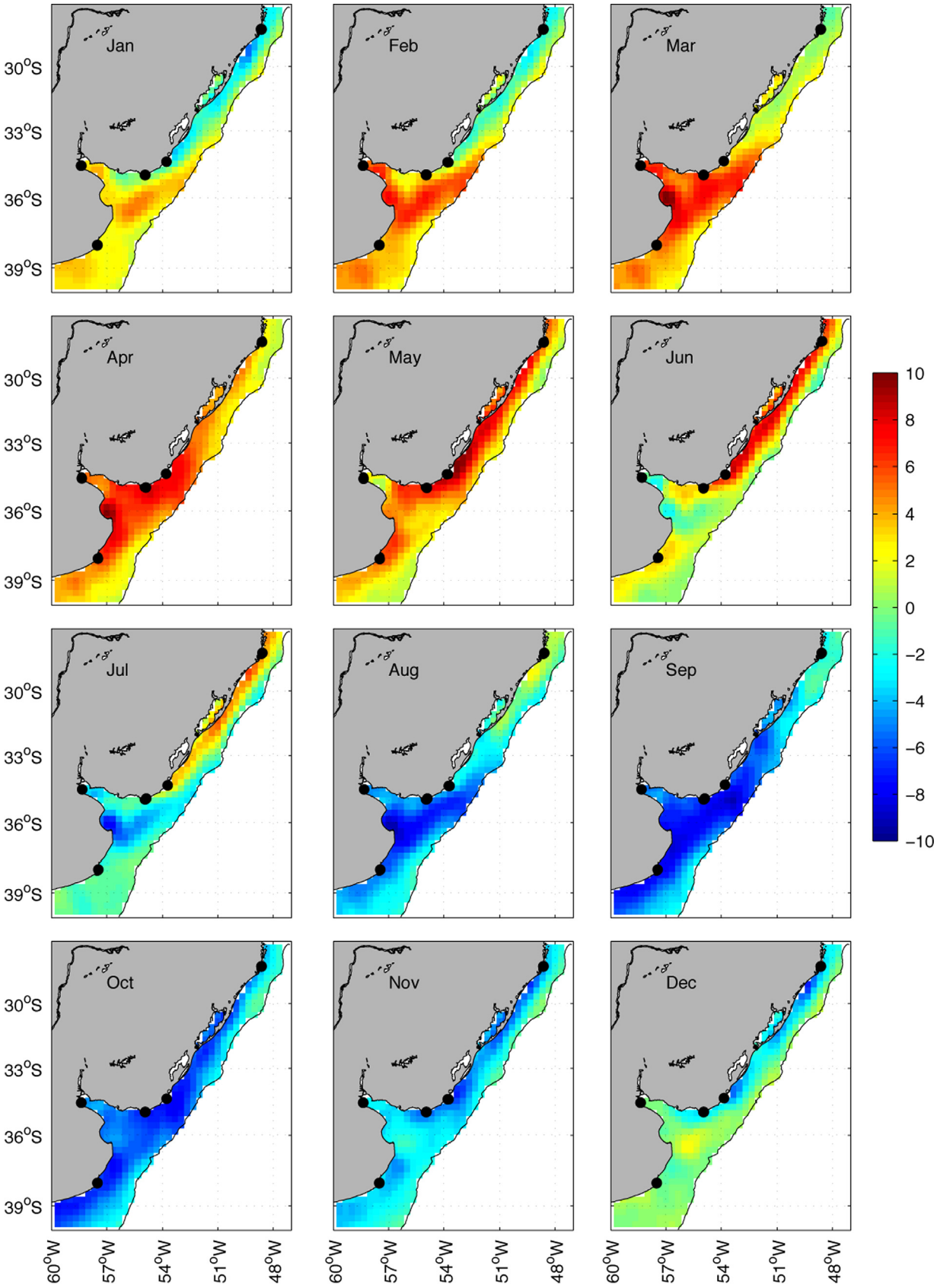

Fig. 11. Climatology of seasonal SLA (cm). Small dots indicate position of the tide gauges (see Fig. 1 for the names). Months are indicated on the top-left corner of each sub-plot.

Finally, to summarize the results of this section and to provide the reader a view of the net effect of the combination of the two main forcings identified for the SLA variability on seasonal time scales, Fig. 11 shows the seasonal component of the SLA as defined in Section 2.4.1 for the twelve months of the year. The north-south seesaw pattern revealed by the PCs (Fig. 7) and depicted by the phase of the seasonal SLA (Fig. 8) is the most conspicuous feature in Fig. 11, and evident during most of the year. Very atypically, all along of the Uruguayan and Brazilian subtropical coasts, the seasonal SLA is negative from the beginning of the austral spring (September) to the end of the summer (March), whereas positive anomalies are observed at higher latitudes during most of this period. In contrast, a positive SLA anomaly is observed along the Uruguayan and Brazilian coasts during the austral fall and early winter (May to July). These features, which can be explained by the dominant upwelling-downwelling favorable winds along the year, are only slightly visible in the SSTs (see, for instance Fig. 7 in Simionato et al., 2010 or Fig. 8 in Campos et al., 2013) but clearly revealed by the altimetry data. Moreover, whereas upwelling can be detected in SST observations, the downwelling revealed by our analysis of the SLA can hardly be observed in those data. This illustrates how satellite-derived SSTs complement SLAs from altimetry.

4. Summary of conclusions

In this paper we present an analysis of the gridded product of satellite SLA in the southeastern South American continental shelf between 27°S and 40°S. We study the variance in the diverse timescales and discuss the associated physical processes. Significant variability is found in all the time scales resolved by satellite altimetry (longer than 20 days): sub-annual, seasonal, interannual and long-term trends. Results show that variability in this region is highly impacted by the fresh water outflows of the RdP estuary and the PL complex as well as by the seasonal modulation of the wind variability.

The seasonal cycle explains a large portion of the variance over most of the study area. The comparison of the evolution of the SLA and SST along the year displays very different features. Remarkably, sea level along the subtropical Uruguayan and Brazilian coasts is higher in fall than in summer. This fact can be explained as the effect of the joint action of the seasonal wind variability and the solar radiation cycle. The combination of both effects accounts for up to 98% of the variance in the seasonal time scale. Natural wind variability and the orientation of the coast forces a regime that changes along the year from upwelling favorable to downwelling favorable, and at different timings along the coast. The seasonal modulation of the synoptic variability of the wind produces this way a north-south dipole pattern, which is responsible for a difference of up to 12 cm between the southern (Argentinean) RdP estuary coast and the Uruguayan and southern Brazilian coasts. This result is confirmed by the analysis of *in-situ* TGs time series that suggest a difference of up to 16 cm.

On interannual time scales, SLA is coherent with the ENSO phenomena. As shown by other articles, during the warm (cold) phase of the ENSO precipitation largely increases (decreases) over the area drained by the RdP and PL. As a consequence, the fresh water outflow also rises (drops), increasing (decreasing) sea level. In addition, during El Niño (La Niña) an easterly (westerly) wind anomaly occurs, which would also be favorable to an increment (reduction) of the sea level in the areas impacted by the plumes.

Finally, SLA also shows a significant positive trend of up to 5 mm yr^{-1} on the shelf, except in an area offshore the PL and in a smaller region of the RdP. The significant positive trend observed close to the continental shelf break could be a consequence of the southward migration of the semi permanent South Atlantic High reported by other authors. In the upper RdP a positive trend of 1–2 mm yr^{-1} is observed, which is consistent with inferences from a 100 year-long TG at Buenos Aires as reported by previous studies.

Beyond the regional significance of the results, this study shows that satellite altimetry data are accurate enough to reveal spatio-temporal patterns near the coast and on the continental shelf of southeastern South America on seasonal and longer time scales. A similar conclusion has been obtained in other coastal areas: Venegas et al. (2008) in the coastal region off Oregon and Léger et al. (2012) in the northern coast of New Guinea found that SLA patterns are consistent with other satellite and *in-situ* independent data.

Acknowledgments

Two anonymous Reviewers and Professor P.T. Strub provided useful comments to improve the article. For SST: NOAA Coast-watch Program, NOAA NESDIS Office of Satellite Data Processing and Distribution, and NASA Goddard Space Flight Center and Ocean Color Web. This study is a contribution to the ANPCyT (National Agency for Scientific and Technological Research of Argentina) PICT 2012 0467, PICT 2010-1831, the CONICET (National Council for Scientific and Technological Research of Argentina) PIP 112 201101 00176, PIP 133 20130100242 CO and the UBACyT 2011-2014 20020100100840 Projects. LRE is supported by grant SGP 2076 from the Inter-American Institute for Global Change Research which is supported by the US National Science Foundation (Grant GEO-0452325).

References

Acha, M., Simionato, C.G., Carozza, C., Mianzan, H., 2012. Climate induced year classes' fluctuations of whitemouth croaker *Micropogonias furnieri* (Pisces, Sciaenidae) in the Río de la Plata estuary, Argentina–Uruguay. Fish. Oceanogr. 21 (1), 58–77. http://dx.doi.org/10.1111/j.1365-2419.2011.00609.x.

Allen, M.R., Smith, L.A., 1996. Monte Carlo SSA: detecting irregular oscillations in the presence of colored noise. J. Clim. 6, 3373–3402.

Barros, V.E., Doyle, M.E., Camillioni, I.A., 2008. Precipitation trends in southeastern South America: relationship with ENSO phases and with low-level circulation. Theor. Appl. Climatol. 93, 19–33. http://dx.doi.org/10.1007/s00704-007-0329.

Broomhead, D.S., King, G.P., 1986. On the qualitative analysis of experimental dynamical systems. In: Sarkar, S. (Ed.), Nonlinear Phenomena and Chaos. Adam Hilger, Bristol, pp. 113–144.

Campos, E.J. D., Lentini, C.A. D., Miller, J.L., Piola, A.R., 1999. Interannual variability of the sea surface temperature in the South Brazil Bight. Geophys. Res. Lett. 26, 2061.

Campos, P.C., Möller Jr., O.O., Piola, A.R., Palma, E.D., 2013. Seasonal variability and coastal upwelling near Cape Santa Marta (Brazil). J. Geophys. Res. Oceans 118, 1420–1433. http://dx.doi.org/10.1002/jgrc.20131.

Chelton, D.B., Schlax, M.G., Samelson, R.M., 2011. Global observations of nonlinear mesoscale eddies. Prog. Oceanogr. 91 (2), 167–216.

Chelton, D., Schlax, M.G., 2003. The accuracies of smoothed sea surface height fields constructed from tandem satellite altimeter datasets. J. Atmos. Oceanic Technol. 20, 1276–1302.

Compagnucci, R.H., Araneo, D., Canziani, P.O., 2001. Principal sequence pattern analysis: a new approach to classifying the evolution of atmospheric systems. Int. J. Climatol. 21, 197–217.

Dettinger, M.D., Ghil, M., Strong, C.M., Weibel, W., Yiou, P., 1995. Software Expedites Singular-spectrum Analysis of Noisy Time Series (12, 14). Eos, Transactions of the American Geophysical Union 76 (2), 21.

D'Onofrio, E.E., Fiore, M.M.E., Pousa, J.L., 2008. Changes in the regime of storm surges at Buenos Aires, Argentina (West Palm Beach (Florida), ISSN 0749-0208). J. Coast. Res. 24 (1A), 260–265. http://dx.doi.org/10.2112/008-NIS.1.

da Silveira, I.C. A., Calado, L., Castro, B.M., Cirano, M., Lima, J.A. M., Mascarenhas, A. d. S., 2004. On the baroclinic structure of the Brazil Current–Intermediate Western Boundary Current system at 22°–23°S. Geophys. Res. Lett. 31, L14308. http://dx.doi.org/10.1029/2004GL020036.

Fernandes, E.H.L., Dyer, K.R., Möller, O.O., Niencheski, L.F.H., 2002. The Patos Lagoon hydrodynamics during an El Niño event (1998). Cont. Shelf Res. 22, 1699–1713.

Fiore, M.M. E., D'Onofrio, E.E., Pousa, J.L., Schnack, E.J., Bértola, G.R., 2009. Storm surges and coastal impacts at Mar del Plata, Argentina. Cont. Shelf Res. 29 (14), 1643–1649.

Framiñan, M.B., 2005. On the Physics, Circulation and Exchange Processes of the Río de la Plata Estuary and the Adjacent Shelf (Doctoral Dissertation). University of Miami, Rosenstiel School of Marine and Atmospheric Science, Miami, Florida, USA 486.

Framiñan, M.B., Etala, M.P., Acha, E.M., Guerrero, R.A., Lasta, C.A., Brown, O.B., 1999. Physical characteristics and processes of the Río de la Plata Estuary. In: Perillo, G.M., Piccolo, M.C., Pino Quivira, M. (Eds.), Estuaries of South America: Their Morphology and Dynamics. Springer, New York, NY, pp. 161–194.

Garcia, A.M., Vieira, J.P., Winemiller, K.O., 2003. Effects of 1997–1998 El Niño on the dynamics of the shallow-water fish assemblage of the Patos Lagoon estuary (Brazil). Estuarine Coast. Shelf Sci. 57, 489–500.

Ghil, M., Allen, R.M., Dettinger, M.D., Ide, K., Kondrashov, D., Mann, M.E., Robertson, A., Saunders, A., Tian, Y., Varadi, F., Yiou, P., 2002. Advanced spectral methods for climatic time series. Rev. Geophys. 40 (1), 3.1–3.41. http://dx.doi.org/10.1029/2000RG000092.

Goni, G.J., Bringas, F., DiNezio, P.N., 2011. Observed low frequency variability of the Brazil Current front. J. Geophys. Res. 116, C10037. http://dx.doi.org/10.1029/2011JC007198.

Guerrero, R.A., Acha, E.M., Framiñan, M.B., Lasta, C.A., 1997. Physical oceanography of the Río de la Plata Estuary, Argentina. Cont. Shelf Res. 17 (7), 727–742.

Han, G., Ikeda, M., Smith, P.C., 1993. Annual variation of sea surface slopes over the Scotian Shelf and Grand Banks from Geosat altimetry. Atmos. Ocean 31 (4), 591–615.

Holgate, S.J., Matthews, A., Woodworth, P.L., Rickards, L.J., Tamisiea, M.E., Bradshaw, E., Foden, P.R., Gordon, K.M., Jevrejeva, S., Pugh, J., 2013. New data systems and products at the permanent service for mean sea level (3). J. Coast. Res. 29, 493–504. http://dx.doi.org/10.2112/JCOASTRES-D-12-00175.1.

Jaime, P., Menéndez, A., Uriburu Quirno, M., Torchio, J., 2002. Análisis del régimen hidrológico de los ríos Paraná y Uruguay (Informe LHA 05-216-02). Instituto Nacional del Agua, Buenos Aires, Argentina.

Jiang, N., Ghil, M., Neelin, D. (1995), Forecasts of equatorial Pacific SST anomalies by using an autoregressive process and singular spectrum analysis. In: Experimental Long-Lead Forecast Bulletin vol. 4, No. 1 (Jan. 1995), pp. 24-27 and subsequent quarterly issues (1995–1997), National Meteorological Center, NOAA, U.S. Department of Commerce.

Jolliffe, I.T., 2002. Principal Component Analysis, second ed.. Springer-Verlag, New York, NY (ISBN 0-387-95442-2, xxix+487 pp).

Kalnay, E., Kanamitsu, M., Kistler, R., Collins, W., Deaven, D., Gandin, L., Iredell, M., Saha, S., White, G., Woollen, J., Zhu, Y., Leetmaa, A., Reynolds, R., Chelliah, M., Ebisuki, W., Higgins, W., Janowiak, J., Mo, K., Ropelewski, C., Wang, J., Jenne, R., Joseph, D., 1996. The NCEP/NCAR 40-year reanalysis project. Bull. Am. Meteorol. Soc. 77, 437–471.

Kimoto, M., Ghil, M., Mo, K.C., 1991. Spatial structure of the extratropical 40-day oscillation (In: Proceedings of the Eighth Conference on Atmospheric and Oceanic Waves and Stability). American Meteorological Society, Boston, MA, pp. 115–116.

Kjerfve, B., 1986. Comparative oceanography of coastal lagoons. In: Wolfe, D.A (Ed.), Estuarine Variability. Academic Press, Orlando, Florida, pp. 63–81.

Lanfredi, N.W., Pousa, J.L., D'Onofrio, E.E., 1998. Sea-level rise and related potential hazards on the Argentine Coast. J. Coastal Res. 14 (1), 47–60.

Le Traon, P.Y., Dibarboure, G., 2002. Velocity mapping capabilities of present and future altimeter missions: the role of high frequency signals. J. Atmos. Oceanic Technol 19, 2077–2088.

Le Traon, P.Y., Faugère, Y., Hernandez, F., Dorandeu, J., Mertz, F., Ablain, M., 2003. Can we merge GEOSAT follow-on with TOPEX/Poseidon and ERS-2 for an improved description of the ocean circulation? J. Atmos. Oceanic Technol. 20, 889–895.

Leeuwenburgh, O., Stammer, D., 2002. Uncertainties in altimetry-based velocity estimates. J. Geophys. Res. (Oceans) 107 (C10), 3175.

Léger, F., Radenac, MH., Dutrieux, P., Menkes C., Eldin, G., 2012. The New Guinea Coastal Current and Upwelling System: Seasonal Variability Inferred from Along-track Altimetry, Surface Temperature and Chlorophyll, 20 years of Progress in Radar Altimetry Symposium, September 24–29, 2012, Venice-Lido, Italy.

Mann, M.E., Park, J., 1999. Advances in Geophysics, vol. 41. Elsevier 239 (pages).

Meccia, V.L., Simionato, C.G., Guerrero, R.A., 2013a. The Rio de la Plata Estuary response to wind variability in synoptic time scale: salinity fields and breakdown and reconstruction of the salt wedge structure. J. Coastal Res. , http://dx.doi.org/10.2112/JCOASTRES-D-11-00063.1.

Meccia, V.L., Simionato, C.G., Fiore, M.E., D'Onofrio, E.E., Dragani, W.C., 2009. Sea surface height variability in the Rio de la Plata estuary from synoptic to interannual scales: results of numerical simulations. Estuarine Coast. Shelf Sci. 85 (2), 327–343.

Meccia, V.L., Simionato, C.G., Guerrero, R., 2013b. The Río de la Plata estuary response to wind variability in synoptic time scale: salinity fields and breakdown and reconstruction of the salt wedge structure. J. Coastal Res. 29 (1), 61–77. http://dx.doi.org/10.2112/JCOASTRES-D-11-00063.1.

Meyssignac, B., Cazenave, A., 2012. Sea level: a review of present-day and recent-past changes and variability. J. Geodyn. 58 (0), 96–109.

Möller Jr, O.O., Piola, A.R., Freitas, A.C., Campos, E.J. D., 2008. The effects of river discharge and seasonal winds on the shelf off southeastern South America. Cont. Shelf Res. 28 (13), 1607–1624.

Möller, O.O., Castello, J.P., Vaz, A.C., 2009. The effect of river discharge and winds on the interannual variability of the pink shrimp Farfantepenaeus paulensis production in Patos Lagoon. Estuaries Coasts 32, 787–796.

Möller, O.O., Fernandes, E., 2010. O Estuario da Lagoa dos Patos: um século de transformaçoes (chapter 2). Ediçao de U. Seeliger, C. Odebrecht, Rio Frande, FURG 180.

Monteiro, I.O., Marques, W.C., Fernandes, E.H., Gonçalves, R.C., Möller Jr., O.O., 2011. On the effect of earth rotation, river discharge, tidal oscillations, and wind in the dynamics of the Patos Lagoon coastal plume. J. Coastal Res. 27 (1), 120–130.

Nagy, G.J., Martínez, C.M., Caffera, R.M., Pedraloza, G., Forbes, E.A., Perdomo A.C., Laborde, J.L., 1997. The hydrological and climatic setting of the Río de la Plata, In: The Río de la Plata, An Environmental Review, An EcoPlata Project Background Report, Dalhausie University, Halifax, Nova Scotia, pp. 17–68.

Pasquini, A.I., Niencheski, L.F.H., Depetris, P.J., 2012. The ENSO signature and other hydrological characteristics in Patos and adjacent coastal lagoons, south-eastern Brazil. Estuarine Coast. Shelf Sci., http://dx.doi.org/10.1016/j.ecss.2012.07.004.

Permanent Service for Mean Sea Level (PSMSL), 2012. "Tide Gauge Data", Retrieved 02 Nov 2011 from ⟨http://www.psmsl.org/data/obtaining⟩.

Pimenta, F., Garvine, R.W., Münchow, A., 2008. Observations of coastal upwelling off Uruguay downshelf of the Plata estuary, South America. J. Mar. Res. 66, 835–872.

Piola, A.R., Campos, E.J. D., Möller Jr., O.O., Charo, M., Martinez, C., 2000. Subtropical shelf front off eastern South America. J. Geophys. Res. 105, 6565–6578.

Piola, A.R., Matano, R.P., Palma, E.D., Möller Jr, O.O., Campos, E.J. D., 2005. The influence of the Plata River discharge on the western South Atlantic shelf. Geophys. Res. Lett. 32 (1), 1–4.

Piola, A.R., Romero, S.I., Zajaczkovski, U., 2008. Space-time variability of the Plata plume inferred from ocean color. Cont. Shelf Res. 28 (13), 1556–1567.

Plaut, G., Vautard, R., 1994. Spells of low-frequency oscillations and weather regimes in the Northern Hemisphere. J. Atmos. Sci. 51, 210–236.

Preisendorfer, R.W., 1988. Principal Component Analysis in Meteorology and Oceanography. Elsevier, Amsterdam 436.

Risien, C.M., Chelton, D.B., 2008. A global climatology of surface wind and wind stress fields from eight years of QuikSCAT Scatterometer Data. J. Phys. Oceanogr. 38 (11), 2379–2413.

Robertson, A.W., Mechoso, C.R., 1998. Interannual and decadal cycles in river flows of southeastern South America. J. Clim. 11, 2570–2581.

Robertson, A.W., Ma, C.-C., Mechoso, C.R., Ghil, M., 1995a. Simulation of the tropical Pacific climate with a coupled ocean-atmosphere general circulation model, Part I: The seasonal cycle. J. Clim. 8, 1178–1198.

Robertson, A.W., Ma, C.-C., Ghil, M., Mechoso, C.R., 1995b. Simulation of the Tropical-Pacific climate with a coupled ocean-atmosphere general circulation model. Part II: Interannual variability. J. Clim. 8, 1199–1216.

Romero, S.I., Piola, A.R., Charo, M., Garcia, C.A. E., 2006. Chlorophyll-a variability off Patagonia based on SeaWiFS data. J. Geophys. Res. 111, C05021.

Ruiz-Etcheverry, L.A., Saraceno, M., Piola, A.R., Valladeau, G., Möller, O.O., 2014. Annual cycle in coastal sea level from gridded satellite altimetry and tide gauges submitted to. Cont. Shelf Res.

Saraceno, M., Provost, C., Piola, A.R., Bava, J., Gagliardini, A., 2004. Brazil Malvinas Frontal System as seen from 9 years of advanced very high resolution radiometer data. J. Geophys. Res. 109, C05027.

Saraceno, M., D,D'Onofrio, E.E., Fiore, M.E., Grismeyer, W.H., 2010. Tide model comparison over the Southwestern Atlantic Shelf. Cont. Shelf Res. 30 (17), 1865–1875.

Saraceno, M., Provost, C., 2012. On eddy polarity distribution in the southwestern Atlantic. Deep Sea Res. Part I 69, 62–69.

Sato, O.T., Polito, P.S., 2008. Influence of salinity on the interannual heat storage trends in the Atlantic estimated from altimeters and Pilot Research Moored Array in the Tropical Atlantic data. J. Geophys. Res. 113, C02008. http://dx.doi.org/10.1029/2007JC004151.

Simionato, C.G., Luz Clara Tejedor, M., Campetella, C., Guerrero, R., Moreira, D., 2010. Patterns of sea surface temperature variability on seasonal to sub-annual scales at and offshore the Río de la Plata estuary. Cont. Shelf Res. 30 (19), 1983–1997.

Simionato, C.G., Meccia, V.L., Guerrero, R.A., Dragani, W.C., Nuñez, M.N., 2007. Río de la Plata estuary response to wind variability in synoptic to intraseasonal scales: 2. Currents' vertical structure and its implications for the salt wedge structure. J. Geophys. Res. 112, C07005. http://dx.doi.org/10.1029/2006JC003815.

Simionato, C.G., Meccia, V.L., Dragani, W.C., Guerrero, R.A., Nuñez, M.N., 2006. The Río de la Plata estuary response to wind variability in synoptic to intraseasonal scales: Barotropic response. J. Geophys. Res. 111 (C09031).

Simionato, C.G., Vera, C.S., Siegismund, F., 2005. Surface wind variability on seasonal and interannual scales over Río de la Plata Area. J. Coastal Res. 21 (4), 770–783.

Simionato, C.G., Dragani, W.C., Meccia, V., Nuñez, M., 2004. A numerical study of the barotropic circulation of the Río de la Plara estuary: sensitivity to bathymetry, Earth rotation and low frequency wind variability. Estuarine Coast. Shelf Sci. 61, 261–273.

Simionato, C.G., Nuñez, M.N., Engel, M., 2001. The salinity front of the Río de la Plata—a numerical case study for winter and summer conditions. Geophys. Res. Lett. 28 (13), 2641–2644.

Smith, W.H.F., Sandwell, D.T., 1997. Global sea floor topography from satellite altimetry and ship depth soundings. Science 277, 1956–1962.

Unal, Y.S., Ghil, M., 1995. Interannual and interdecadal oscillation patterns in sea level. Clim. Dyn. 11, 255–278.

Vautard, R., Yiou, P., Ghil, M., 1992. Singular-spectrum analysis: a toolkit for short, noisy chaotic signals. Physica D 58, 95–126.

Vautard, R., Ghil, M., 1989. Singular spectrum analysis in nonlinear dynamics, with applications to paleoclimatic time series. Physica D 35, 395–424.

Venegas, R.M., Ted Strub, P., Beier, E., Letelier, R., Thomas, A.C., Cowies, T., James, C., Soto-Mardones, L., Cabrera, C., 2008. Satellite-derived variability in chlorophyll, wind stress, sea surface height, and temperature in the northern California current system. J. Geophys. Res. C: Oceans 113, 3.

Volkov, D.L., Larnicol, G., Dorandeu, J., 2007. Improving the quality of satellite altimetry data over continental shelves. J. Geophys. Res. 112 (C06020).

Wöppelmann, G., Marcos, M., Santamaría-Gómez, A., Martín-Míguez, B., Bouin, M.-N., Gravelle, M., 2014. Evidence for a differential sea level rise between hemispheres over the twentieth century. Geophys. Res. Lett., 41. http://dx.doi.org/10.1002/2013GL059039.